nature electronics

ARTICLES

https://doi.org/10.1038/s41928-018-0114-0

Trochoidal motion and pair generation in skyrmion and antiskyrmion dynamics under spin–orbit torques

Ulrike Ritzmann[1,2]*, Stephan von Malottki[3], Joo-Von Kim[4], Stefan Heinze[3], Jairo Sinova[1,5] and Bertrand Dupé[1]

Magnetic skyrmions are swirling magnetic spin structures that could be used to build next-generation memory and logic devices. They can be characterized by a topological charge that describes how the spin winds around the core. The dynamics of skyrmions and antiskyrmions, which have opposite topological charges, are typically described by assuming a rigid core. However, this reduces the set of variables that describe skyrmion motion. Here we theoretically explore the dynamics of skyrmions and antiskyrmions in ultrathin ferromagnetic films and show that current-induced spin–orbit torques can lead to trochoidal motion and skyrmion–antiskyrmion pair generation, which occurs only for either the skyrmion or antiskyrmion, depending on the symmetry of the underlying Dzyaloshinskii–Moriya interaction. Such dynamics are induced by core deformations, leading to a time-dependent helicity that governs the motion of the skyrmion and antiskyrmion core. We compute the dynamical phase diagram through a combination of atomistic spin simulations, reduced-variable modelling and machine learning algorithms. It predicts how spin–orbit torques can control the type of motion and the possibility to generate skyrmion lattices by antiskyrmion seeding.

Two-dimensional spin structures such as vortices and skyrmions[1,2] possess a non-trivial topology that affords them a degree of stability[3–5]. These structures are characterized by a topological winding number or 'charge',

$$q = -\frac{1}{4\pi}\int \mathrm{d}^2 r\, \mathbf{m}\cdot\left(\frac{\partial \mathbf{m}}{\partial x}\times\frac{\partial \mathbf{m}}{\partial y}\right) \quad (1)$$

where $\mathbf{m}=\mathbf{m}(\mathbf{r},t)$ is a unit vector representing the orientation of the magnetic moments in time and space. Skyrmions ($q=1$) and antiskyrmions ($q=-1$), for example, possess opposite charges and can appear in pairs through the continuous deformation of the uniform state ($q=0$)[6–8]. The description of the dynamics of skyrmions and antiskyrmions can be approximated by assuming a rigid core, which leads to a reduced set of variables describing their motion. These dynamics are captured by the Thiele equation[9],

$$\mathbf{G}\times\frac{\partial \mathbf{X}}{\partial t}+\alpha D_0\frac{\partial \mathbf{X}}{\partial t}=\mathbf{F} \quad (2)$$

which describes the damped gyrotropic motion of the (anti)skyrmion core position, $\mathbf{X}$, in response to a force $\mathbf{F}$. Here $\mathbf{G}=-qG_0\mathbf{z}$ is the gyrovector, α is a damping constant and D_0 is a structure factor related to the damping (see Methods). While the dynamics in equation (2) is non-Newtonian, the gyrotropic response depends on q (that is, its topology) and dictates the direction in which the core moves. This conceptual framework has been useful to understand vortex dynamics[10,11], spin-torque vortex oscillators[12,13] and the current-driven motion of skyrmions[6,7,14–18].

In most studies to date, however, the robustness of the symmetry between opposite topological charges, as expressed in equation (2), has not been examined in detail. In particular, the roles of core deformation beyond inertial effects[19], the internal degrees of freedom and the underlying symmetry of the magnetic interactions that stabilize the skyrmions remain an open question. This issue is of particular importance since nanometre-scale skyrmions are desirable for possible device applications[20,21] and antiskyrmions have been observed in Heusler compounds[22] and predicted to occur at transition metal interfaces[23,24].

In this Article, we show that the symmetries of the magnetic interactions, combined with spin–orbit torques (SOTs), play an important role in determining how the (anti)skyrmion core moves. In particular, the choice of the Dzyaloshinskii–Moriya interaction (DMI) can lead to qualitatively different motion for opposite q charges. Namely, deviations from rectilinear motion and skyrmion–antiskyrmion pair generation can occur above certain SOT thresholds for the skyrmion or the antiskyrmion depending on the choice of DMI.

Atomistic spin dynamics simulations

To explore this issue in greater depth, we studied theoretically the spin dynamics of skyrmions and antiskyrmions in an ultrathin 3*d* transition metal ferromagnet on a 5*d* normal metal substrate as shown in Fig. 1a. A prominent example of this material combination is PdFe/Ir(111), where a large DMI is induced in the Fe monolayer through interfacial coupling to the strong spin–orbit interaction in the Ir substrate[25,26]. This allows individual

[1]Institute of Physics, Johannes Gutenberg University Mainz, Mainz, Germany. [2]Department for Physics and Astronomy, Uppsala University, Uppsala, Sweden. [3]Institute of Theoretical Physics and Astrophysics, Christian-Albrechts-Universität zu Kiel, Kiel, Germany. [4]Centre de Nanosciences et de Nanotechnologies, CNRS, Univ. Paris-Sud, Université Paris-Saclay, Palaiseau, France. [5]Institute of Physics, Academy of Sciences of the Czech Republic, Prague, Czech Republic. *e-mail: ulrike.ritzmann@physics.uu.se

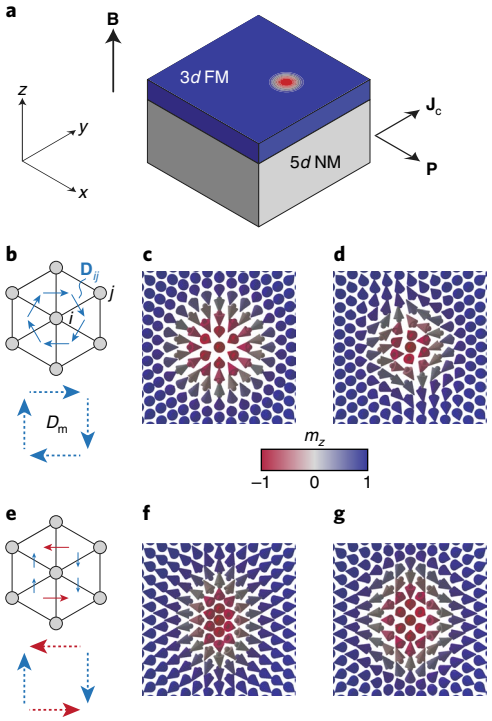

Fig. 1 | Film geometry, symmetry of the DMI and skyrmion profiles. **a**, The bilayer system studied comprising an ultrathin 3*d* transition metal ferromagnet (FM) on a 5*d* normal metal (NM) substrate, with the configuration of the applied magnetic field (**B**), charge current ($\mathbf{J}_c$) and effective spin polarization vector (**P**). **b**, The hexagonal lattice structure and orientation of the DMI $\mathbf{D}_{ij}$ used in the atomistic spin dynamics simulations. The dashed arrows represent the effective Dzyaloshinskii–Moriya vectors $\mathbf{D}_m$ in the continuum (micromagnetic) limit. **c**, The equilibrium skyrmion ($q=1$) configuration with the DMI in **b**. **d**, The equilibrium antiskyrmion ($q=-1$) configuration with the DMI in **b**. **e**, The hexagonal lattice structure and orientation of the modified DMI vectors used to favour the antiskyrmion state. The dashed arrows represent the effective Dzyaloshinskii–Moriya vectors $\mathbf{D}_m$ in the continuum limit. **f**, The equilibrium skyrmion ($q=1$) configuration with the DMI in **e**. **g**, The equilibrium antiskyrmion ($q=-1$) configuration with the DMI in **e**.

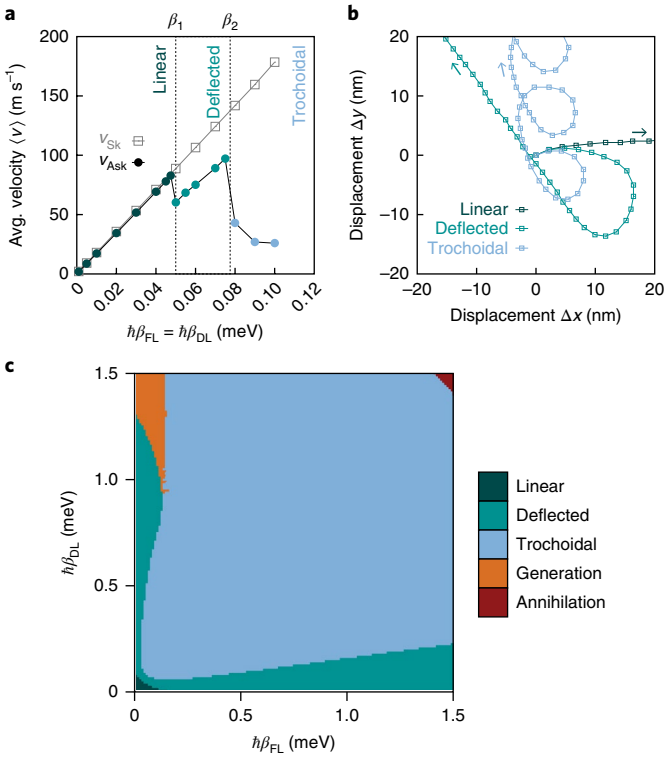

Fig. 2 | Motion of antiskyrmions under current-induced SOTs. **a**, Variation of the average velocity $\langle v\rangle$ of skyrmions and antiskyrmions as a function of SOT, where $\beta_{FL}=\beta_{DL}$. Three propagation regimes are identified for antiskyrmions: rectilinear motion at low currents; deflected motion at intermediate currents; and trochoidal motion at high currents. **b**, An example of antiskyrmion trajectories for linear ($\hbar\beta_{FL}=\hbar\beta_{DL}=0.04$ meV), deflected ($\hbar\beta_{FL}=\hbar\beta_{DL}=0.06$ meV) and trochoidal motion ($\hbar\beta_{FL}=\hbar\beta_{DL}=0.09$ meV). The arrows indicate the propagation direction. **c**, The β_{FL}–β_{DL} phase diagram for the antiskyrmion dynamics.

skyrmions to exist as metastable states, which has been brought to light in recent experiments[27]. Moreover, it has been shown that a variety of antiskyrmion states ($q=-1$, -2) are also metastable when frustrated exchange interactions are taken into account in such ultrathin films[28–31] and more generally in bulk chiral magnets[32,33], which lead to an attractive interaction between skyrmions[34]. We employed density functional theory calculations to obtain estimates of the exchange, anisotropy, and DMI energies for PdFe/Ir(111), which were then used to parametrize an atomistic spin model for studying the dynamics (see Methods). Minimizing this energy allows us to determine the equilibrium spin configuration of the static skyrmion and antiskyrmion profiles, as shown in Fig. 1c,d, respectively. Note that the exchange and DMI possess a six-fold symmetry that is consistent with the Ir(111) surface (Fig. 1b).

The spin dynamics are computed by time-integrating the Landau–Lifshitz–Gilbert equation with additional SOT terms due to the applied current,

$$\frac{\mathrm{d}\mathbf{m}}{\mathrm{d}t}=-\frac{1}{\hbar}\mathbf{m}\times\mathbf{B}_{\mathrm{eff}}+\alpha\mathbf{m}\times\frac{\mathrm{d}\mathbf{m}}{\mathrm{d}t}+\beta_{\mathrm{FL}}\mathbf{m}\times\mathbf{P}+\beta_{\mathrm{DL}}\mathbf{m}\times(\mathbf{m}\times\mathbf{P}) \quad (3)$$

where $\hbar$ is the reduced Planck constant, $\mathbf{B}_{\mathrm{eff}}=-\delta H/\delta\mathbf{m}$ is the effective field, α is the Gilbert damping constant, β_{FL} is the strength of the field-like torque and β_{DL} is the strength of the damping-like torque. $\mathbf{P}=\hat{\mathbf{x}}$ is the orientation of the effective spin polarization, which models an applied electric current along the *y* direction in the film plane (Fig. 1a). While in-plane currents should, in principle, flow through both the ferromagnet and normal metal substrate, we assume that the majority of the current flows only through the substrate since the layer resistivity is significantly larger for the ultrathin ferromagnet (one or two monolayers thick), given the importance of interfacial scattering[35] and its relative thickness in comparison to the substrate. We can therefore neglect spin transfer torques generated within the 3*d* ferromagnet and assume only field-like and damping-like contributions from the spin–orbit coupling in the 5*d* substrate.

Dynamics and skyrmion–antiskyrmion pair generation

An example of the ensuing current-driven motion of a skyrmion is shown in Fig. 2a, where the average velocity is plotted as a function of the SOT for the case of $\beta_{FL}=\beta_{DL}$. This behaviour is consistent with the Thiele equation, which predicts a linear variation of the skyrmion velocity as a function of the SOT[14] (see Supplementary Video 1). In contrast to skyrmions, the average velocity of antiskyrmions does not increase monotonically with the SOT (Fig. 2a). A linear regime is found at low currents up to a first threshold, β_1, where a discontinuity in the velocity curve can be seen. Above this threshold, the velocity continues to increase linearly as a function of β but with a different slope. A second threshold β_2 is found as the

strength of the SOT is increased, where the velocity decreases with the applied current. The calculated trajectories for the antiskyrmion core are presented in Fig. 2b. For linear motion, we observe that the spin configuration of the core is slightly deformed but remains close to its equilibrium static configuration (see Supplementary Video 2). Above the first threshold β_1, the trajectory is linear at long times but exhibits a large transient phase in which the motion is curved. The rotation ceases when a new steady-state regime is reached, which then allows for linear motion to proceed indefinitely (albeit with a different Hall angle with respect to the linear case $\beta<\beta_1$; see Supplementary Video 3). More interestingly, the core undergoes trochoidal motion for $\beta>\beta_2$ that comprises an average displacement along a line that is accompanied by oscillations resulting in loops along the trajectory (see Supplementary Video 4). The onset of these oscillations results in the sharp decrease in the average velocity shown in Fig. 2a. The phase diagram of the different behaviour is shown in Fig. 2c for different values and ratios of β_{FL} and β_{DL}. We used algorithms based on machine learning to classify the three types of trajectory (linear, deflected and trochoidal), which exhibit a wide range of velocities and propagation directions (see Methods). We note that the trochoidal motion occurs over a wide range of SOT parameters.

The deflected and trochoidal motion are driven by deformations to the antiskyrmion core. This deformation is characterized by the emergence of a dynamical variable $\psi(t)$ that describes the helicity of the skyrmion and antiskyrmion (Fig. 3a). For skyrmions, ψ describes the continuous transition between Bloch and Néel states of opposite chirality, while for antiskyrmions it describes the rotation of the Bloch or Néel axes. In our system, the deformation is driven by the SOT, which results in a tilt in the magnetization in the film plane, characterized by an amplitude η and the azimuthal angle ϕ_t, that depends on the relative strength between the field-like and damping-like terms. This tilt is uniform for the background spins, while it varies within the antiskyrmion core depending on the orientation of ψ. By assuming a suitable ansatz for the deformation profile (see Methods, Supplementary Note 1 and Supplementary Figs. 1–3), we can derive an equation of motion for $\psi(t)$ using a Lagrangian approach,

$$D_\psi \frac{\partial \psi}{\partial t} = \sigma_\psi \hbar \beta_{DL} \eta \cos(\phi_p - \phi_t) - \frac{\partial U}{\partial \psi} \quad (4)$$

where D_ψ is a damping structure factor, σ_ψ is an SOT efficiency factor, ϕ_p is the azimuthal angle of the spin polarization vector $\mathbf{P}$ ($\phi_p=0$ in the simulations) and U is the internal magnetic energy. We note that a similar expression was found for channelled skyrmion motion through edge states[18]. As the effective SOT force acting on $\mathbf{X}(t)$ in equation (2) can be written as

$$\mathbf{F} = \sigma_0 \hbar \beta_{DL} (\sin(\psi - \phi_p), q\cos(\psi - \phi_p)) \quad (5)$$

the dynamics of ψ determines the time dependence of the force and therefore the overall trajectory of the antiskyrmion as shown in Fig. 2b, and results from the interplay between the SOT term σ_ψ and the restoring force governed by $\partial_\psi U$. The SOT therefore induces a coupling between the translational dynamics of the core with its helicity, a feature that has been seen previously in frustrated magnets[31]. We verified this interpretation by computing the spatially resolved forces from the atomistic spin simulations (see Supplementary Note 2 and Supplementary Figs. 4 and 5). In Fig. 3b,c, we present $U(\psi)$ extracted from the spin dynamics simulations for different SOT strengths. We find that the potential can be described accurately by the function $U(\psi)=u_1\cos(\psi-\psi_0)+u_3\cos(3\psi)$, where $u_1\propto\eta^2$ and $\psi_0\propto 2\phi_t$ for antiskyrmions, which is consistent with predictions from the model (see Methods). The u_3 term represents a lattice effect that accounts for the underlying hexagonal lattice structure[36] and is found to be largely independent of the SOT. The position of the energy minimum is largely independent of the SOT for $\beta_{FL}=\beta_{DL}$ because the tilt ϕ_t remains almost constant for this torque ratio (Fig. 3b). However, cases where $\beta_{FL}\neq\beta_{DL}$ lead to different values of ϕ_t, which results in a shift in the minimum (see Supplementary Note 3 and Supplementary Fig. 6).

From $U(\psi)$, we can understand the salient features of equation (4) as follows. For low amplitudes of the SOT, the restoring force due to the lattice term u_3 dominates and the steady-state value of ψ remains close to its equilibrium value $\psi\simeq 0$, resulting in the simple

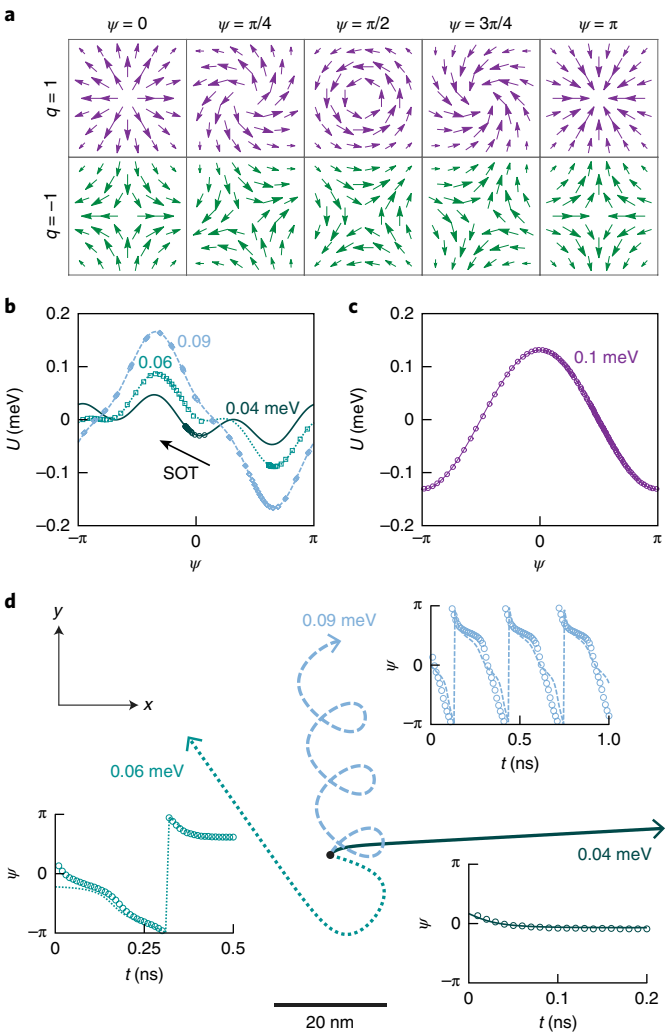

Fig. 3 | Helicity dynamics in the extended Thiele model. a, Spin configurations at the skyrmion ($q=1$) and antiskyrmion ($q=-1$) core for different values of the helicity parameter, ψ. **b**, The antiskyrmion energy $U(\psi)$ for different values of $\beta_{FL}=\beta_{DL}$, where the figures denote the SOT strength in millielectronvolts. Three regimes are shown: linear (0.04 meV), deflected (0.06 meV) and trochoidal (0.09 meV). The open symbols represent data extracted from spin dynamics simulations, while the lines represent fits to the function $U(\psi)=u_1\cos(\psi-\psi_0)+u_2\cos(3\psi)$. The arrow indicates schematically the SOT force. **c**, $U(\psi)$ for a skyrmion with the DMI constant D_{ij} reduced by a factor of 10^3, for which the trochoidal regime is attained for $\hbar\beta_{FL}=\hbar\beta_{DL}=0.1$ meV. **d**, Trajectories for $\beta_{FL}=\beta_{DL}$ using equations (2) and (4) with the fits for $U(\psi)$ in **b**. The insets show $\psi(t)$ extracted from simulations (circles) and computed using equation (4) with the fitted $U(\psi)$ in **b** (lines).

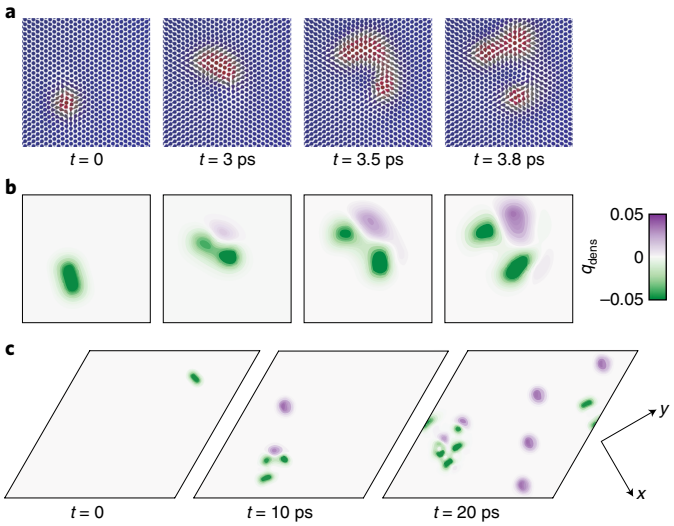

Fig. 4 | Skyrmion–antiskyrmion pair generation from trochoidal antiskyrmion dynamics. a, Snapshots of the trochoidal motion of a single antiskyrmion, where large deformations in the spin structure of the core lead to the nucleation of a skyrmion–antiskyrmion pair. **b**, Topological charge density q_{dens} corresponding to the spin states in **a**. **c**, Snapshots in time of skyrmion–antiskyrmion pair generation, where pairs are nucleated and annihilated periodically. Antiskyrmions that survive become subsequent sources of pair generation. For all snapshots, $\hbar\beta_{FL} = 0.01$ meV and $\hbar\beta_{DL} = 1.35$ meV.

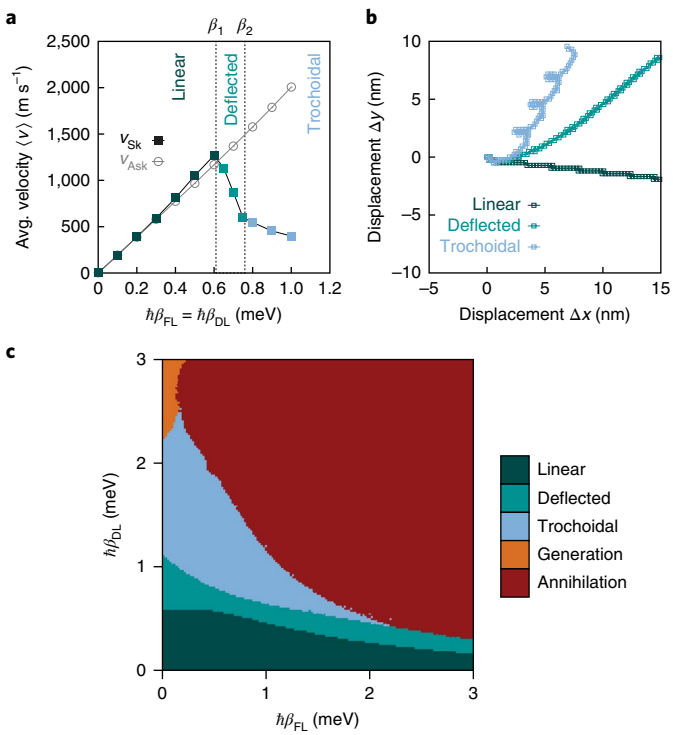

Fig. 5 | Skyrmion and antiskyrmion dynamics with an anisotropic DMI. a, Variation of the velocity of skyrmions and antiskyrmions as a function of the torques, where $\beta_{FL} = \beta_{DL}$, for the DMI shown in Fig. 1e. **b**, Example of skyrmion trajectories for linear ($\hbar\beta_{FL} = \hbar\beta_{DL} = 0.5$ meV), deflected ($\hbar\beta_{FL} = \hbar\beta_{DL} = 0.7$ meV) and trochoidal motion ($\hbar\beta_{FL} = \hbar\beta_{DL} = 0.8$ meV). **c**, β_{FL}–β_{DL} phase diagram for the skyrmion motion.

linear motion expected from equation (2) alone. As the strength of the SOT is increased, the deformation-induced contribution u_1, which is also governed by the DMI, increases and leads to a change in stability, where a new steady-state value $\psi = \psi_0$ is reached. This results in the deflected motion, which is characterized by large transients in $\psi(t)$ leading to the stationary value ψ_0 at long times. This transition between two equilibrium ψ_0 states is hysteretic, which can be seen by sweeping the current above and below the threshold β_1 (see Supplementary Fig. 7). As the SOT is further increased, the trochoidal regime is attained when the SOT contribution exceeds the maximum value of the restoring force $|\partial_\psi U|$, which results in a periodic solution in $\psi(t)$. In this light, the transition toward the trochoidal regime is analogous to Walker breakdown in domain wall motion[37], where the magnetization angle at the domain wall centre plays the role of ψ here. By using the fits in Fig. 3b, we computed the dynamics of $\psi(t)$ using equation (4) to determine the antiskyrmion trajectories in the three regimes (Fig. 3d). We note that the predicted dynamics of $\psi(t)$ and $\mathbf{X}(t)$ accurately reproduce the behaviour obtained from the atomistic spin dynamics simulations described by equation (3) (see Supplementary Fig. 8). These results also illustrate why such transitions are not seen for the skyrmion under similar conditions; Fig. 3c shows that similar variations in $U(\psi)$ can be obtained for a skyrmion only if the DMI constant is reduced by a factor of 10^3, which indicates that the equilibrium skyrmion state is robust and remains largely unperturbed under SOT in this geometry.

Two other regimes beyond the single-particle description are also identified in Fig. 2c. First, under large field-like and damping-like torques, the propagating antiskyrmion is no longer stable and becomes annihilated. Second, and more interestingly, a transition toward another dynamical regime is found under small β_{FL} and large β_{DL}, where deflected or trochoidal motion leads to a periodic generation of skyrmion–antiskyrmion pairs. An example of this process is given in Fig. 4. This regime is strongly nonlinear and represents a complete breakdown of the single-particle picture described by equations (2) and (4) (see Supplementary Notes 4 and 5, and Supplementary Figs. 9 and 10). The pair is generated as follows: as the antiskyrmion undergoes its trochoidal trajectory, it is accompanied by a large deformation that represents an elongation of the core (that is, at $t = 3$ ps in Fig. 4a), similar to the dynamics seen for gyrating magnetic vortices close to the core reversal transition[38–40]. This elongation, which represents a skyrmion–antiskyrmion pair with a net charge of $q = 0$, then separates from the core itself ($t = 3.5$ to 3.8 ps). The corresponding topological charge density q_{dens} for these processes is shown in Fig. 4b. Once nucleated, the pair itself separates since the SOTs lead to different motion for the skyrmion and antiskyrmion constituents. The skyrmion propagates away from the nucleation site by undergoing rectilinear motion, while the nucleated antiskyrmion executes trochoidal motion and becomes itself a new source of pair generation. This phenomenon leads to the generation of a gas of skyrmions and antiskyrmions (Fig. 4c); the relative population of the two species varies in time as collisions between skyrmions and antiskyrmions lead to annihilation, while pair generation continues for antiskyrmions that survive (see Supplementary Video 5). This process suggests that it is possible to generate an indefinite number of skyrmions and antiskyrmions from a single antiskyrmion 'seed'. Combined with the attractive interaction between cores made possible by the frustrated exchange, this dynamics can eventually lead to a skyrmion 'crystallite' that condenses from the disordered gas phase (see Supplementary Fig. 11). This behaviour is very different to skyrmion generation reported previously, where single pairs are nucleated from static defects through the coupling between local magnetization gradients and spin transfer torques, in systems where skyrmions or antiskyrmions are unstable (depending on the choice of DMI)[7,8].

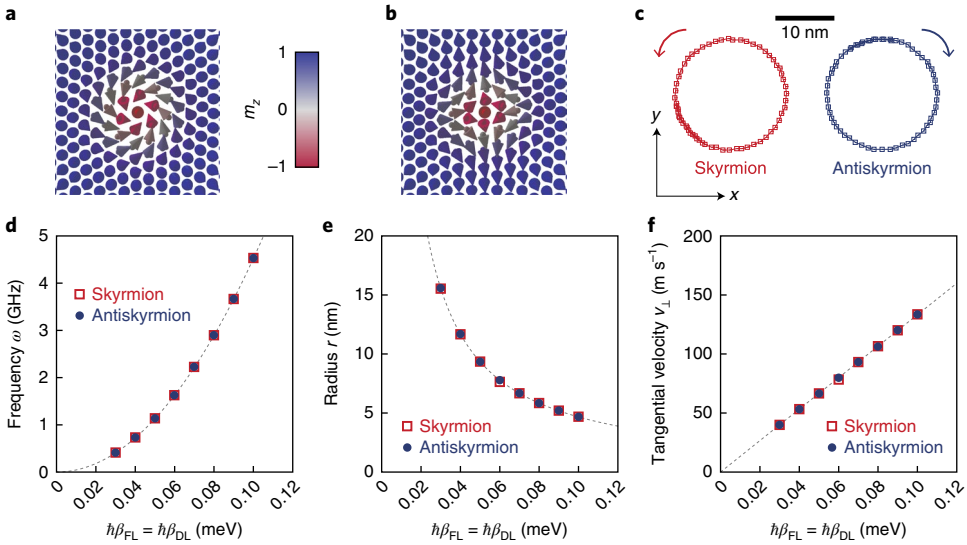

Fig. 6 | Skyrmion and antiskyrmion dynamics without DMI. a, Equilibrium spin configuration of the skyrmion. **b**, Equilibrium spin configuration of the antiskyrmion. **c**, An example of trajectories of skyrmion and antiskyrmion motion for $\hbar\beta_{FL} = \hbar\beta_{DL} = 0.05$ meV. **d**, SOT dependence of the frequency of the circular motion, where the dashed line represents a quadratic fit. **e**, SOT dependence of the radius of the circular motion, where the dashed line represents a reciprocal fit. **f**, Tangential velocity of skyrmions and antiskyrmions as a function of SOT with $\beta_{FL} = \beta_{DL}$, where the dashed line represents a linear fit.

Dynamics under different DMI symmetries

Recall that we observed deflected and trochoidal motion only for antiskyrmions because the energy barriers $U(\psi)$ in the helicity ψ are orders of magnitude larger for skyrmions than for antiskyrmions for the same DMI constant (Fig. 3). As such, the asymmetry between opposite topological charges is related to the form of the underlying DMI, rather than the sign of the charge itself. To test this hypothesis we conducted simulations in which an anisotropic form of the DMI is used instead, whereby the original six-fold symmetry is retained for the exchange interactions while a two-fold symmetry is used for the DMI, the DMI strength along the two axes being different as shown in Fig. 1e. This mimics the symmetry of the DMI induced at a (110) interface[23]. Since the amplitudes of the magnetic interactions are unchanged but only the symmetry is changed, the stability of the magnetic textures is only qualitatively affected. Most importantly, antiskyrmions are favoured energetically over skyrmions for this anisotropic form of the DMI.

Figure 5 summarizes the current-driven dynamics of skyrmions and antiskyrmions with the anisotropic DMI in Fig. 1e. In Fig. 5a, the current dependence of the velocity is shown for the skyrmion and antiskyrmion, whose static profiles are shown in Fig. 1f,g, respectively. In contrast to the behaviour shown in Fig. 2, the antiskyrmion undergoes only rectilinear motion while the skyrmion exhibits deflected and trochoidal motion as the strength of the SOTs is increased. We note that the associated thresholds, β_1 and β_2, are also much higher, where velocities beyond 1 km s^{-1} can be reached in the linear regime for both skyrmions and antiskyrmions. In Fig. 5b, examples of trajectories for the linear, deflected and trochoidal motion for skyrmions are shown. We note that the overall skyrmion Hall angles are different from the antiskyrmion case shown in Fig. 2b, which originates from different stationary values of ψ for the skyrmion. This is a consequence of $U(\psi)$ for the skyrmion with the anisotropic DMI, which possesses a different ψ-dependence from the case shown in Fig. 3b. This difference is also reflected in the (β_{FL}, β_{DL}) phase diagram in Fig. 5c; while the same phases are identified, the overall shape of the phase boundaries differs and certain transitions are absent, such as the transition between deflected motion and pair generation. Nevertheless, the order in which the phases appear with increasing SOT is similar.

The importance of the DMI symmetry can be highlighted further by examining the current-driven dynamics in the absence of DMI altogether. Skyrmions and antiskyrmions remain metastable states because of the frustrated exchange interactions, resulting in the equilibrium profiles shown in Fig. 6a,b. The absence of a chiral interaction results in Bloch and Néel states being degenerate. $U(\psi) = U_0$ is a constant in equation (4), so the internal mode $\psi(t)$ becomes a Goldstone mode of the system that can be excited with vanishingly small torques. The Bloch-like skyrmion profile in Fig. 6a is therefore only one possible realization of the metastable state. For a finite deformation $\eta \neq 0$, $\psi(t) = \omega t$ according to equation (4) and generates a harmonic SOT force in equation (2), which results in circular motion. This has been reported in a previous theoretical study of skyrmions and antiskyrmions in frustrated ferromagnets, in which the dipole–dipole interaction breaks the degeneracy of the different helicity configurations. Therefore, the circular motion can be observed only above a certain threshold, but shows also an opposite sense of rotation for opposite topological charges[32]. This is confirmed in the spin dynamics simulations as shown in Fig. 6c, where circular motion is indeed found with an opposite sense of rotation for opposite topological charges, as expected from the sign of the gyrovector **G** in equation (2). Since the deformation is linear in SOT for the range of values considered, we expect a quadratic variation in the gyration frequency as a function of SOT from equation (4). This is confirmed in Fig. 6d, where the simulated frequencies are well described by a quadratic function. A similar analysis predicts that the radius of gyration should be inversely proportional to the SOT, which is again confirmed by simulations as shown in Fig. 6e. Finally, the SOT dependence of the tangential velocity is presented in Fig. 6f, where a linear variation is found in agreement with theory. Besides the opposite sense of gyration, these results show that the skyrmion and antiskyrmion trajectories agree quantitatively within the numerical accuracy of the simulations.

Conclusions

These results highlight the rich dynamical behaviour that is possible under SOTs in ultrathin ferromagnetic films, especially for metastable chiral states that are not necessarily the most energetically favourable. The work also links skyrmion dynamics to other

known phenomena in micromagnetism, namely Walker breakdown in domain wall motion (trochoidal motion) and vortex core reversal (pair generation). Given the primacy of the DMI symmetry in governing the particle dynamics, our work may spur new avenues of research in materials science where specific surface or interface orientations could be chosen to tailor particular dynamical properties, such as deflected or trochoidal motion, which is absent in most approaches where the focus is on quantifying and controlling rectilinear motion for skyrmion memory and logic applications. The prospect of generating different dynamics with a variety of metastable states within the same material system could also offer new possibilities for studying particle interactions and developing new application paradigms, notably skyrmion generation with a single antiskyrmion 'seed'. Recent theoretical work shows that such seeds are likely to appear at finite temperatures[29] and therefore offer a reliable and efficient means of producing skyrmions and antiskyrmions readily.

Methods

Hamiltonian. The magnetic Hamiltonian studied is given by

$$H=-\sum_{\langle ij\rangle}J_{ij}\mathbf{m}_i\cdot\mathbf{m}_j-\sum_{\langle ij\rangle}\mathbf{D}_{ij}\cdot(\mathbf{m}_i\times\mathbf{m}_j)-\sum_i K(\mathbf{m}_i\cdot\hat{\mathbf{z}})^2-\sum_i\mathbf{B}\cdot\mu_s\mathbf{m}_i \quad (6)$$

where the first term represents the Heisenberg exchange interaction, the second term represents the DMI, the third term represents the uniaxial anistropy along the z axis and the last term represents the Zeeman energy associated with an external field $\mathbf{B}$. The indices $\langle ij\rangle$ in the summation for the exchange and DMI terms indicate that single-site terms are neglected. The moments are assumed to reside on a hexagonal lattice and $|\mathbf{m}_i|=1$ everywhere. The parameters are extracted from density functional theory calculations of the bilayer PdFe system on Ir(111)[26,28], in which we consider a face-centred cubic stacking for the Pd layer. For the Heisenberg exchange, J_{ij} represents the exchange constant between the magnetic moments $\mathbf{m}_i$ and $\mathbf{m}_j$, where up to 10 nearest neighbours are taken into account: $J_1=14.73$ meV, $J_2=-1.95$ meV, $J_3=-2.88$ meV, $J_4=0.32$ meV, $J_5=0.69$ meV, $J_6=0.01$ meV, $J_7=0.01$ meV, $J_8=0.13$ meV, $J_9=-0.14$ meV and $J_{10}=-0.28$ meV. We treat the DMI in the nearest-neighbour approximation as shown in Fig. 1b,e, where a magnitude of 1.0 meV for $\mathbf{D}_{ij}$ is obtained from density functional theory calculations. The anisotropy constant is $K=0.7$ meV and we used an applied magnetic field of 20 T along the z direction. The magnetic moment of the Fe atoms is given by $\mu_s=2.7\mu_B$, with μ_B being the Bohr magneton. For the given parameters, the system is in a ferromagnetic ground state close to the transition point to the skyrmion lattice phase, where isolated skyrmions and antiskyrmions can be stabilized. The applied magnetic field is only slightly larger than the critical field B_c, with $B=1.06B_c$.

Atomistic spin dynamics simulations. The simulation geometry comprises a hexagonal lattice of 100×100 spins with periodic boundary conditions. The ferromagnet is assumed to be one monolayer thick. The dynamics of the spin system described by equation (6) is solved by numerical time integration of the Landau–Lifshitz equation with Gilbert damping and SOTs given in equation (3). We used a Gilbert damping constant of $\alpha=0.3$ for all of the simulations presented here. The numerical time integration is performed using the Heun method. At the start of each simulation, an equilibrium skyrmion or antiskyrmion profile is first computed by relaxing the system in the absence of the SOT terms. This procedure produces the profiles shown in Figs. 1c,d,f,g and 6a,b. The simulations are then executed over several nanoseconds with a fixed time step in the range of 0.1–10 fs.

Extension to the Thiele model. The extension to the Thiele model, expressed by equation (4), is based on the idea that SOTs lead to a significant deformation of the skyrmion/antiskyrmion core. The model is based on two assumptions. First, we assume that all spins in the system are canted toward the film plane under the combined action of the field-like and damping-like SOT. The deformation is assumed to take the form $\mathbf{m}=\mathbf{m}_0+\eta\delta\mathbf{m}$, where the relaxed ground state is $\mathbf{m}_0=(\sin\theta_0\cos\phi_0, \sin\theta_0\cos\phi_0, \cos\theta_0)$ and

$$\delta m_x=\cos^2\theta_0\cos\phi_0\cos(\phi_0-\phi_t)+\sin\phi_0\sin(\phi_0-\phi_t),$$
$$\delta m_y=\cos^2\theta_0\sin\phi_0\cos(\phi_0-\phi_t)-\cos\phi_0\sin(\phi_0-\phi_t),$$
$$\delta m_z=\frac{1}{2}sin2\theta_0\cos(\phi_0-\phi_t)$$

with η representing the amplitude of the deformation and ϕ_t describing the azimuthal component of the background spins that tilt away from the z axis as a result of the SOT. Second, in addition to the core position $\mathbf{X}(t)=(X(t), Y(t))$, we elevate the helicity parameter $\psi(t)$ to a dynamical variable, which is defined through the azimuthal angle $\phi_0(\mathbf{r},t)=q\tan^{-1}[(y-Y(t))/(x-X(t))]+\psi(t)$, where $q=\pm1$ is the topological charge. On the basis of this deformation ansatz, we derive the equation of motion for $\psi(t)$ using a Lagrangian approach[41], which involves a continuum approximation for the magnetization, $\mathbf{m}(\mathbf{r},t)$, with $|\mathbf{m}|=1$. By neglecting coupling terms proportional to η, we derive the Euler–Lagrange equations leading to equations (2) and (4), where the gyrovector term is given by

$$G_0=2\pi\int_0^\infty dr\frac{\partial\theta_0}{\partial r}\sin\theta_0(r) \quad (7)$$

the damping factors are

$$D_0=\pi\int_0^\infty dr\left[r\left(\frac{\partial\theta_0}{\partial r}\right)^2+\frac{1}{r}\sin^2\theta_0(r)\right] \quad (8)$$

$$D_\psi=2\pi\int_0^\infty dr\ r\sin^2\theta_0(r) \quad (9)$$

and the SOT efficiency factors are

$$\sigma_0=\pi\int_0^\infty dr\left[r\frac{\partial\theta_0}{\partial r}+\frac{1}{2}\sin2\theta_0(r)\right] \quad (10)$$

$$\sigma_\psi=2\pi\int_0^\infty dr\ r\sin^2\theta_0(r)\cos\theta_0(r) \quad (11)$$

Here, the equilibrium (anti)skyrmion core profile is assumed to possess a cylindrical symmetry, with r being the radial variable in cylindrical coordinates.

Expressions for the helicity-dependent energy, $U(\psi)$, can be found in a similar way by using the continuum approximation of equation (6). The dominant contribution comes from the DMI. For the symmetry considered in Fig. 1b, we use the form[42,43]

$$U_{DM}=D\int d^2r\left(m_z\frac{\partial m_x}{\partial x}-m_x\frac{\partial m_z}{\partial x}+m_z\frac{\partial m_y}{\partial y}-m_y\frac{\partial m_z}{\partial y}\right) \quad (12)$$

where D is the DMI constant. For skyrmions, we find

$$U_S(\psi)=D(u_{0,S}+\eta^2u_{1,S})\cos\psi \quad (13)$$

where

$$u_{0,S}=2\pi\int_0^\infty dr\left(r\frac{\partial\theta_0}{\partial r}+\frac{1}{2}\sin2\theta_0(r)\right) \quad (14)$$

$$u_{1,S}=\pi\int_0^\infty dr\left(r\frac{\partial\theta_0}{\partial r}\cos^2\theta_0(r)+\frac{3}{4}\sin2\theta_0(r)-\frac{1}{8}\sin4\theta_0(r)\right) \quad (15)$$

Here, $u_{0,S}$ is the dominant term, while the deformation-induced contribution $u_{1,S}$ provides a correction that increases quadratically with the deformation. Only the deformation-induced contribution appears for the antiskyrmion,

$$U_{AS}(\psi)=D\eta^2u_{1,AS}\cos(\psi-2\phi_t) \quad (16)$$

where

$$u_{1,AS}=\frac{\pi}{16}\int_0^\infty dr\left(4r\frac{\partial\theta_0}{\partial r}(1+3\cos2\theta_0(r))+6\sin2\theta_0(r)+\sin4\theta_0(r)\right) \quad (17)$$

As noted in the main text, an additional energy term $\propto\cos(3\psi)$ is required to describe the atomistic simulations, which arises from discretization effects due to the underlying hexagonal lattice. This lattice term is not present in the continuum description.

Classification of skyrmion and antiskyrmion trajectories. The deflected and trochoidal motion for antiskyrmions (with the DMI in Fig. 1b) and skyrmions (with the DMI in Fig. 1e) can involve a wide range of speeds, propagation directions and gyration frequencies. Classifying these behaviours efficiently from simulation data to construct the phase diagrams shown in Fig. 2c and 5c is therefore a challenging task. We employed algorithms based on machine learning to classify these trajectories, which were then used with adaptive meshing to identify the different phase boundaries. First, we excluded the annihilation and pair-generation states from the simulation data, which could be identified directly from the magnetization

state. Second, the velocity orientations within each simulation run for the remaining data were mapped onto the unit circle, which then served as inputs for classification. The linear motion results in a small cluster of points on the circle, the deflected motion gives a partially filled circle, and the trochoidal motion results in a fully filled circle. A subset of these images (5–10 per state) were then used as learning rules to train the Classify function in the technical computing software MATHEMATICA (version 11.2), which was then used to classify the remaining states. The target resolutions of the phase boundaries in Fig. 2c and 5c are 0.01 meV and 0.02 meV, respectively. A brute force search would therefore require 22,500 (150×150) simulation runs for each DMI symmetry, while our iterative method combined with machine learning required only 1,831 (Fig. 2c) and 2,736 (Fig. 5c) runs, respectively. Given that each simulation run takes 5 to 10 h of computation time on a single central processing unit core, our method provides a more efficient way to explore the parameter space of the dynamical system.

Code availability. The codes used during the current study are available from the corresponding author on reasonable request.

Data availability. The data sets generated and/or analysed during the current study are available from the corresponding author on reasonable request.

Received: 6 April 2018; Accepted: 11 July 2018;
Published online: 13 August 2018

References

1. Bogdanov, A. & Yablonskii, D. Contribution to the theory of inhomogeneous states of magnets in the region of magnetic-field-induced phase transitions. Mixed state of antiferromagnets. *Zh. Eksp. Teor. Fiz.* **69**, 142–146 (1989).
2. Bogdanov, A. & Hubert, A. The stability of vortex-like structures in uniaxial ferromagnets. *J. Magn. Magn. Mater.* **195**, 182–192 (1999).
3. Hagemeister, J., Romming, N., Von Bergmann, K., Vedmedenko, E. Y. & Wiesendanger, R. Stability of single skyrmionic bits. *Nat. Commun.* **6**, 8455 (2015).
4. Rohart, S., Miltat, J. & Thiaville, A. Path to collapse for an isolated Néel skyrmion. *Phys. Rev. B* **93**, 665–666 (2016).
5. Stosic, D., Mulkers, J., Van Waeyenberge, B., Ludermir, T. B. & Milošević, M. V. Paths to collapse for isolated skyrmions in few-monolayer ferromagnetic films. *Phys. Rev. B* **95**, 214418 (2017).
6. Koshibae, W. & Nagaosa, N. Theory of antiskyrmions in magnets. *Nat. Commun.* **7**, 10542 (2016).
7. Everschor-Sitte, K., Sitte, M., Valet, T., Abanov, A. & Sinova, J. Skyrmion production on demand by homogeneous DC currents. *New J. Phys.* **19**, 092001 (2017).
8. Stier, M., Häusler, W., Posske, T., Gurski, G. & Thorwart, M. Skyrmion–anti-skyrmion pair creation by in-plane currents. *Phys. Rev. Lett.* **118**, 267203 (2017).
9. Thiele, A. A. Steady-state motion of magnetic domains. *Phys. Rev. Lett.* **30**, 230 (1973).
10. Guslienko, K. Y. et al. Eigenfrequencies of vortex state excitations in magnetic submicron-size disks. *J. Appl. Phys.* **91**, 8037 (2002).
11. Choe, S. B. et al. Vortex core-driven magnetization dynamics. *Science* **304**, 420–422 (2004).
12. Ivanov, B. & Zaspel, C. Excitation of spin dynamics by spin-polarized current in vortex state magnetic disks. *Phys. Rev. Lett.* **99**, 247208 (2007).
13. Mistral, Q. et al. Current-driven vortex oscillations in metallic nanocontacts. *Phys. Rev. Lett.* **100**, 257201 (2008).
14. Sampaio, J., Cros, V., Rohart, S., Thiaville, A. & Fert, A. Nucleation, stability and current-induced motion of isolated magnetic skyrmions in nanostructures. *Nat. Nanotech.* **8**, 839–844 (2013).
15. Nagaosa, N. & Tokura, Y. Topological properties and dynamics of magnetic skyrmions. *Nat. Nanotech.* **8**, 899–911 (2013).
16. Lin, S.-Z., Reichhardt, C., Batista, C. D. & Saxena, A. Driven skyrmions and dynamical transitions in chiral magnets. *Phys. Rev. Lett.* **110**, 207202 (2013).
17. Lin, S.-Z. & Hayami, S. Ginzburg–Landau theory for skyrmions in inversion-symmetric magnets with competing interactions. *Phys. Rev. B* **93**, 064430 (2016).
18. Leonov, A. O. & Mostovoy, M. Edge states and skyrmion dynamics in nanostripes of frustrated magnets. *Nat. Commun.* **8**, 14394 (2017).
19. Büttner, F. et al. Dynamics and inertia of skyrmionic spin structures. *Nat. Phys.* **11**, 225–228 (2015).
20. Fert, A., Cros, V. & Sampaio, J. Skyrmions on the track. *Nat. Nanotech.* **8**, 152–156 (2013).
21. Fert, A., Reyren, N. & Cros, V. Magnetic skyrmions: advances in physics and potential applications. *Nat. Rev. Mater.* **2**, 17031 (2017).
22. Nayak, A. K. et al. Magnetic antiskyrmions above room temperature in tetragonal Heusler materials. *Nature* **548**, 561–566 (2017).
23. Hoffmann, M. et al. Antiskyrmions stabilized at interfaces by anisotropic Dzyaloshinskii–Moriya interaction. *Nat. Commun.* **8**, 308 (2017).
24. Güngördü, U., Nepal, R., Tretiakov, O. A., Belashchenko, K. & Kovalev, A. A. Stability of skyrmion lattices and symmetries of quasi-two-dimensional chiral magnets. *Phys. Rev. B* **93**, 064428 (2016).
25. Fert, A. & Levy, P. M. Role of anisotropic exchange interactions in determining the properties of spin-glasses. *Phys. Rev. Lett.* **44**, 1538–1541 (1980).
26. Dupé, B., Hoffmann, M., Paillard, C. & Heinze, S. Tailoring magnetic skyrmions in ultra-thin transition metal films. *Nat. Commun.* **5**, 4030 (2014).
27. Romming, N. et al. Writing and deleting single magnetic skyrmions. *Science* **341**, 636–639 (2013).
28. Dupé, B., Kruse, C. N., Dornheim, T. & Heinze, S. How to reveal metastable skyrmionic spin structures by spin-polarized scanning tunneling microscopy. *New J. Phys.* **18**, 055015 (2016).
29. Böttcher, M., Heinze, S., Egorov, S., Sinova, J. & Dupé, B. B-T phase diagram of Pd/Fe/Ir(111) computed with parallel tempering Monte Carlo. Preprint at https://arxiv.org/abs/1707.01708 (2018).
30. von Malottki, S., Dupé, B., Bessarab, P. F., Delin, A. & Heinze, S. Enhanced skyrmion stability due to exchange frustration. *Sci. Rep.* **7**, 12299 (2017).
31. Leonov, A. O. & Mostovoy, M. Multiply periodic states and isolated skyrmions in an anisotropic frustrated magnet. *Nat. Commun.* **6**, 8275 (2015).
32. Zhang, X. et al. Skyrmion dynamics in a frustrated ferromagnetic film and current-induced helicity locking-unlocking transition. *Nat. Commun.* **8**, 1717 (2017).
33. Hu, Y., Chi, X., Li, X., Liu, Y. & Du, A. Creation and annihilation of skyrmions in the frustrated magnets with competing exchange interactions. *Sci. Rep.* **7**, 16079 (2017).
34. Rózsa, L. et al. Skyrmions with attractive interactions in an ultrathin magnetic film. *Phys. Rev. Lett.* **117**, 157205 (2016).
35. Sondheimer, E. H. The mean free path of electrons in metals. *Adv. Phys.* **50**, 499–537 (2001).
36. Rózsa, L. et al. Formation and stability of metastable skyrmionic spin structures with various topologies in an ultrathin film. *Phys. Rev. B* **95**, 094423 (2017).
37. Slonczewski, J. C. Theory of domain-wall motion in magnetic films and platelets. *J. Appl. Phys.* **44**, 1759–1770 (1973).
38. Van Waeyenberge, B. et al. Magnetic vortex core reversal by excitation with short bursts of an alternating field. *Nature* **444**, 461–464 (2006).
39. Yamada, K. et al. Electrical switching of the vortex core in a magnetic disk. *Nat. Mater.* **6**, 270–273 (2007).
40. Gaididei, Y., Kravchuk, V. P. & Sheka, D. D. Magnetic vortex dynamics induced by an electrical current. *Int. J. Quantum Chem.* **110**, 83–97 (2010).
41. Kim, J.-V. in *Solid State Physics* (eds Camley, R. E. & Stamps, R. L.) 217–294 (Academic, San Diego, 2012).
42. Bogdanov, A. N. & Rößler, U. K. Chiral symmetry breaking in magnetic thin films and multilayers. *Phys. Rev. Lett.* **87**, 037203 (2001).
43. Thiaville, A., Rohart, S., Jué, É., Cros, V. & Fert, A. Dynamics of Dzyaloshinskii domain walls in ultrathin magnetic films. *Europhys. Lett.* **100**, 57002 (2012).

Acknowledgements

This work was partially supported by the Horizon2020 Framework Programme of the European Commission under grant no. 665095 (MAGicSky). J.-V.K. acknowledges support from the Deutscher Akademischer Austauschdienst under award no. 57314019. U.R. acknowledges support from the Deutsche Forschungsgemeinschaft (grant RI2891/1-1). U.R., B.D. and J.S. acknowledge the Alexander von Humboldt Foundation, the Deutsche Forschungsgemeinschaft (grant DU1489/2-1), the Graduate School of Excellence Materials Science in Mainz (MAINZ), the ERC Synergy Grant SC2 (no. 610115), the Transregional Collaborative Research Center (SFB/TRR) 173 SPIN+X and the Grant Agency of the Czech Republic (grant no. 14-37427G).

Author contributions

B.D. and S.H. initiated the project. U.R. and S.v.M. developed the atomistic spin dynamics code and U.R. performed the atomistic spin dynamics simulations. U.R. and J.-V.K. interpreted the simulation results and developed the analytical model. S.H., B.D., J.-V.K. and U.R. wrote the manuscript. All of the authors discussed the data.

Competing interests

The authors declare no competing interests.

Additional information

Supplementary information is available for this paper at https://doi.org/10.1038/s41928-018-0114-0.

Reprints and permissions information is available at www.nature.com/reprints.

Correspondence and requests for materials should be addressed to U.R.

Publisher's note: Springer Nature remains neutral with regard to jurisdictional claims in published maps and institutional affiliations.